CFD-PBE modelling of continuous Ni-Mn-Co hydroxide co-precipitation for Li-ion batteries

(Article begins on next page)

18 October 2022

CFD-PBE modelling of continuous Ni-Mn-Co hydroxide co-precipitation for Li-ion batteries

Mohsen Shiea*, Andrea Querio, Antonio Buffo, Gianluca Boccardo, Daniele Marchisio

Dipartimento di Scienza Applicata e Tecnologia, Politecnico di Torino, Corso Duca degli Abruzzi 24, 10129 Torino, Italy

ABSTRACT

A modelling framework is proposed to simulate the co-precipitation of Ni-Mn-Co hydroxide as precursor of cathode material for lithium-ion batteries. It integrates a population balance equation with computational fluid dynamics to describe the evolution of the particle size in (particularly continuous) co-precipitation processes. The population balance equation is solved by employing the quadrature method of moments. In addition, a multi-environment micromixing model is employed to consider the potential effect of molecular mixing on the fast co-precipitation reaction. The modelling framework is used to investigate the co-precipitation of $Ni_{0.8}Mn_{0.1}Co_{0.1}(OH)_2$ in a multi-inlet vortex micromixer, as a suitable candidate for the study of fast co-precipitation processes in continuous mode. Finally, the simulation results are discussed, and the role of the different phenomena involved in the formation and evolution of particles is identified by inspecting the predicted trends.

© 2021 The Authors. Published by Elsevier B.V. on behalf of Institution of Chemical Engineers. This is an open access article under the CC BY-NC-ND license (http://creativecommons.org/licenses/by-nc-nd/4.0/).

1. Introduction

Lithium-ion batteries are growing exponentially in diverse applications, such as electric portable devices and appliances, electric vehicles, and stationary energy storage systems, due to their versatility and high energy density in comparison to other secondary battery technologies. This growth has been driving a considerable amount of research toward developing batteries of desired characteristics, e.g., larger capacity, higher energy density, longer life-time, greater safety and lower environmental impact. It is well-known that these decisive characteristics are determined by the cathode properties, which in turn are inherited from the cathode's precursor material. In this regard, layered nickel-manganese-cobalt based materials are one of the most interesting cathodes for lithium-ion batteries due to their high capacity, and structural and thermal stability. The precursor material of these cathodes

is nickel-manganese-cobalt hydroxide, which is produced mainly by the co-precipitation in continuous stirred tank reactors (CSTR). The knowledge about the co-precipitation of $Ni_{1-x-y}Mn_xCo_y(OH)_2$ is of fundamental importance for the sake of process scale-up and product optimization. For instance, it is desired to understand the effect of the operating conditions on the final particle properties, e.g., the mean particle size, broadness of the distribution and particle tap density, as required for controlling particle quality in manufacturing processes. In this regard, there exists a substantial number of experimental researches that study the co-precipitation of $Ni_{1-x-y}Mn_xCo_y(OH)_2$, mainly in CSTRs with long residence time (Lee et al., 2004; Deng et al., 2008; Van Bommel and Dahn, 2009; Kim et al., 2011; Yang et al., 2015). In contrast, few works have been dedicated to the simulation of this process. Barai and co-workers (Barai et al., 2019), for instance, simulated the co-precipitation of $Ni_{1/3}Mn_{1/3}Co_{1/3}(OH)_2$ in a stirred

semi-batch reactor, i.e., with no outflow. They adopted a multi-scale computational approach to describe the nucleation, growth of primary particles and their subsequent aggregation into secondary particles. However, no coupling between the fluid dynamics and evolution of particles is present in the modelling. In another example, Liu et al. (Liu et al., 2021) presented a numerical modelling of $Ni_{0.6}Mn_{0.2}Co_{0.2}(OH)_2$ co-precipitation in a Taylor-Couette flow reactor. The modelling framework includes the CFD, i.e., fluid dynamics governing equations, and a micromixing model. However, no method is used to predict the evolution of the particle properties, e.g., size. We believe that this aspect deserves more attention because a predictive simulation tool can be beneficial for the purpose of the process optimization and scale-up by reducing the need for expensive and time-consuming experiments.

In this work, we present a comprehensive approach based on the Computational Fluid Dynamics (CFD) and Population Balance Modelling (PBM) to simulate the co-precipitation of $Ni_{0.8}Mn_{0.1}Co_{0.1}(OH)_2$ in a multi-inlet vortex micromixer (MIVM). In this approach, the CFD provides the information about the flow and total concentration fields, while the PBM describes the formation and evolution of particles through particle processes such as nucleation, growth and aggregation. In addition, the approach includes an equilibrium solver to determine the chemical state of the supersaturated solution. A multi-environment micromixing model is also included to take into account the molecular segregation of the feed solutions. Regarding the choice of the case study, there are several reasons behind choosing the MIVM. On one hand, it is a continuous system operating at steady-state conditions, and therefore, the proposed approach is useful for the simulation of other continuous reactors such as CSTRs. On the other hand, this system has been leveraged to study mixing-controlled co-precipitation processes (Marchisio et al., 2008; Liu et al., 2008; Cheng and Fox, 2010; Lince et al., 2011; Bensaid et al., 2014), and is a suitable experimental setup for the development of reliable models by using, for instance, optimization techniques.

2. Modelling of $Ni_{0.8}Mn_{0.1}Co_{0.1}(OH)_2$ co-precipitation

The synthesis of Ni-Mn-Co hydroxide is carried out by the reaction of the metal sulfates with sodium hydroxide under the presence of ammonia as the chelating agent (Lee et al., 2004). The reactions involved are shown in Table 1 (Van Bommel and Dahn, 2009).

The co-precipitation is triggered by the chemical reactions involved, which result in a supersaturated solution, i.e., a solution with the activity of the metal hydroxides higher than their solubility product. The generated supersaturation, in turn, induces the nucleation and growth of particles, which can eventually aggregate to form larger particles. The formation and evolution of particles by nucleation, growth and aggregation can be described by a population balance equation (Marchisio et al., 2003). Simultaneously, the total concentration of the reactants in the bulk fluid is tracked by coupling the chemical species balance equations with the population balance equation (PBE). Moreover, the microscale segregation of the feed streams is taken into account by a turbulent micromixing model. In the following, the main aspects of the modelling framework is discussed in detail.

2.1. Micromixing model

In the case of fast reactions, the injection of the reactants from different inlets can result in segregation at the molecular scale (i.e., microscale), hence slowing down the involved reactions. This can have a considerable effect on the reaction rate, and therefore, it should be considered in the modelling framework (Pohorecki and Baldyga, 1983). In this work, we use the multi-environment micromixing model that treats the segregation by defining environments that interact together and that corresponds to a presumed functional form for the corresponding composition probability density function (Fox, 1998). At a given time and spatial position, each environment is described by a probability (or volume fraction) and local concentrations of the involved species in that environment. We adopt the simplest arrangement of environments by associating one environment to each feed solution, which then mix to form a reacting/precipitation environment. Thus, there are three feed environments corresponding to the metal, sodium hydroxide and ammonia feeds, and one environment in which the co-precipitation can occur. In the multi-environment micromixing model, the concentration of each feed environment is assumed to be constant, but their probability decreases as they mix to form the precipitation environment. The probability of the feed environments is tracked by (Fox, 1998):

$$\frac{\partial p_i}{\partial t} + \mathbf{u}_f \cdot \frac{\partial p_i}{\partial \mathbf{x}} = \frac{\partial}{\partial \mathbf{x}} \cdot \left(\Gamma_t \frac{\partial p_i}{\partial \mathbf{x}} \right) - r_i \quad \text{for} \quad i \in \{1, 2, 3\}, \tag{1}$$

where p_i is the volume fraction of the i-th environment, r_i the probability flux from the i-th environment to the precipitation environment due to the micromixing, $\mathbf{u}_f$ is the velocity of the particles, identical to that of the fluid due to the very small particle size, and Γ_t is the turbulent diffusivity. The probability of the precipitation environment, p_4, is instead calculated by

$$p_4 = 1 - \sum_{i=1}^{3} p_i, \tag{2}$$

since the sum of all probabilities must be equal to unity. The probability fluxes are defined as follows (Fox, 1998):

$$r_i = \gamma p_i (1 - p_i) \quad \text{for} \quad i \in \{1, 2, 3\}, \tag{3}$$

where the choice of γ determines the micromixing rate and in turbulent flows is usually expressed in terms of the local turbulence fields. Here, it is modelled by the following expression (Marchisio et al., 2001):

$$\gamma = C_f \frac{C_\phi}{2} \frac{\varepsilon}{\kappa}, \tag{4}$$

where κ and ε are the turbulent kinetic energy and dissipation rate, respectively. In addition, C_f and C_ϕ are modeling coefficients. In flows characterized by high Reynolds numbers, C_ϕ is set to 2. However, Liu and Fox (Liu and Fox, 2006) argued that this value overestimates the micromixing rate, in the case of $Sc = \nu/\Gamma \gg 1$ (e.g., in liquids), and they developed a correlation for C_ϕ that depends on the local turbulent Reynolds number ($Re_l = \kappa/\sqrt{\varepsilon\nu}$):

$$C_\phi = \sum_{n=1}^{6} a_n (\log_{10} Re_l)^n, \tag{5}$$

Table 1 – Equilibrium reactions involved in the co-precipitation of Ni$_{0.8}$Mn$_{0.1}$Co$_{0.1}$(OH)$_2$ (Van Bommel and Dahn, 2009).	
Reactions	Notes
$M_i^{2+} + NH_3 \rightleftharpoons [M_i(NH_3)]^{2+}$ $M_i^{2+} + 2\,NH_3 \rightleftharpoons [M_i(NH_3)_2]^{2+}$ $M_i^{2+} + 3\,NH_3 \rightleftharpoons [M_i(NH_3)_3]^{2+}$ $M_i^{2+} + 4\,NH_3 \rightleftharpoons [M_i(NH_3)_4]^{2+}$ $M_i^{2+} + 5\,NH_3 \rightleftharpoons [M_i(NH_3)_5]^{2+}$ $M_i^{2+} + 6\,NH_3 \rightleftharpoons [M_i(NH_3)_6]^{2+}$ $M_i^{2+} + 2\,OH^- \rightleftharpoons M_i(OH)_2$ $NH_3 + H_2O \rightleftharpoons NH_4^+ + OH^-$ $H_2O \rightleftharpoons H^+ + OH^-$	–$i \in \{1, 2, 3\}$; $M_1^{2+} \equiv Ni^{2+}$, $M_2^{2+} \equiv Mn^{2+}$, $M_3^{2+} \equiv Co^{2+}$ –Nickel and cobalt form all the six complexes, while manganese forms only the first four complexes

where ν is the liquid kinematic viscosity and Γ the species molecular diffusivity. The coefficients a_n are taken from the work of Liu and Fox (Liu and Fox, 2006). In addition, the correction coefficient C_f is added to Eq. (4) to match the scalar dissipation rate predicted by the multi-environment model and that calculated by assuming a fully developed scalar spectrum in turbulent flows (Marchisio et al., 2001). More information about this correction coefficient is reported in the Supplementary Material.

2.2. Governing equations in precipitation environment

In this work, the particles are assumed to move with the fluid velocity without disturbing the fluid flow field, because their size is sufficiently small (as discussed in Section 3) and their volume fraction is low. In addition, the sole particle property of interest is size (L). Thus, a statistical description of the particle population can be provided by the particle size distribution (PSD) that defines the expected number density of particles in the joint space of the particle size and physical domain. The evolution in the physical space and time of the PSD $n(L)$ is described by the PBE. Here, the quadrature method of moments (QMOM) is adopted to solve the PBE (Marchisio et al., 2001). In this approach, the PSD is approximated by a summation of N weighted Dirac delta functions, each located at a quadrature abscissa. Then, the problem of solving the PBE is reduced to tracking $2N$ (usually low order) moments of the PSD. The moment of order k is defined as:

$$m_k = \int_0^\infty L^k n(L) dL. \tag{6}$$

With the assumption that particles are precipitated only in the precipitation environment, the following transport equation is written for the volume-weighted moments of that environment, $\langle m_k^{(4)} \rangle = p_4 m_k^{(4)}$, (Marchisio et al., 2002):

$$\frac{\partial \langle m_k^{(4)} \rangle}{\partial t} + \mathbf{u}_f \cdot \frac{\partial \langle m_k^{(4)} \rangle}{\partial \mathbf{x}} = \frac{\partial}{\partial \mathbf{x}} \cdot \left(\Gamma_t \frac{\partial \langle m_k^{(4)} \rangle}{\partial \mathbf{x}} \right) + p_4 h_k^{(4)}, \tag{7}$$

where $h_k^{(4)}$ is the source term of k-order moment due to the nucleation, growth and aggregation:

$$h_k^{(4)} = J L_c^k + k G m_{k-1}^{(4)} + \bar{B}_k^a - \bar{D}_k^a, \tag{8}$$

here, J is the nucleation rate, G the growth rate and L_c the nuclei size. In addition, $\bar{B}_k^a$ and $\bar{D}_k^a$ denote, respectively, the particle birth and death rates due to the aggregation. In the context of QMOM, the contribution of aggregation to changing k-order

moment, $\left(\bar{B}_k^a - \bar{D}_k^a \right)$, is expressed as follows (Marchisio et al., 2003):

$$\left(\bar{B}_k^a - \bar{D}_k^a \right) = \sum_{i=1}^N \sum_{j=1}^N w_i^{(4)} w_j^{(4)} \beta_{ij} P_{ij} \left[\frac{1}{2} \left(L_i^3 + L_j^3 \right)^{(k/3)} - L_i^k \right], \tag{9}$$

where, β_{ij} and P_{ij} denote, respectively, the collision rate and aggregation efficiency between two particles of size L_i and L_j. Moreover, $w_i^{(4)}$ and L_i are the weight and abscissa of the i-th quadrature node. They are found by applying an inversion algorithm to moments of the precipitation environment, $m_k^{(4)}$, (Marchisio and Fox, 2013).

As described later, the models for J, G and P_{ij} depend on the local conditions, i.e., chemical species activities in the precipitation environment. Thus, the moment transport equations should be coupled with the following transport equations for the volume-weighted total concentrations, $s_\alpha^{(4)} = p_4 c_{T,\alpha}^{(4)}$, of nickel, manganese, cobalt, ammonia, sodium and sulfate:

$$\frac{\partial s_\alpha^{(4)}}{\partial t} + \mathbf{u}_f \cdot \frac{\partial s_\alpha^{(4)}}{\partial \mathbf{x}} = \frac{\partial}{\partial \mathbf{x}} \cdot \left(D_{\text{eff}} \frac{\partial s_\alpha^{(4)}}{\partial \mathbf{x}} \right) + \sum_{i=1}^3 r_i c_{T,\alpha}^{(i)} + p_4 Q_\alpha^{(4)}, \tag{10}$$

here, D_{eff} is the effective diffusivity, i.e., summation of the molecular and turbulent diffusivities, for the species. In addition, $Q_\alpha^{(4)}$ is the sink term for the reactants that are consumed in the co-precipitation, i.e., nickel, manganese and cobalt. It is calculated from the generated volume of the precipitate, that is $h_3^{(4)}$, by assuming the spherical shape for particles. Lastly, the term $\sum_{i=1}^3 r_i c_{T,\alpha}^{(i)}$ represents the flux of species α from the feed environment i to the reacting one, due to micromixing. It is worth mentioning that the total concentration of species in each feed environment, denoted here by $c_{T,\alpha}^{(i)}$, is constant and equal to that of the corresponding inlet feed stream.

In order to solve Eq. (7), models are used to describe the nucleation, growth and aggregation of particles. First the supersaturation needs to be calculated, which is the measure of the co-precipitation driving force. In the context of this work, the supersaturation is defined as the ratio of the product of the activity coefficients of the involved ions and the Ni$_{0.8}$Mn$_{0.1}$Co$_{0.1}$(OH)$_2$ solubility product (Mersmann, 2001):

$$S = \sqrt[3]{\frac{(a_{Ni^{2+}})^{0.8} (a_{Mn^{2+}})^{0.1} (a_{Co^{2+}})^{0.1} (a_{OH^-})^2}{\left(k_{sp}^{Ni(OH)_2} \right)^{0.8} \left(k_{sp}^{Mn(OH)_2} \right)^{0.1} \left(k_{sp}^{Co(OH)_2} \right)^{0.1}}}, \tag{11}$$

where, a and k_{sp} denote the chemical activity and solubility product, respectively. The activities are calculated by solving a system of non-linear equations representing the involved chemical equilibria, excluding that of the co-precipitation, as

explained in Section 2.3. The values of k_{sp} in Eq. (11) are taken from the work by Van Bommel and Dahn (2009).

For the nucleation model, we adopt the following expression based on the classical nucleation theory (Volmer and Weber, 1926):

$$J = k_1 \exp\left(\frac{-B_1}{(\ln S)^2}\right) + k_2 \exp\left(\frac{-B_2}{(\ln S)^2}\right), \qquad (12)$$

which contains two contributions accounting for homogeneous and heterogeneous nucleation. Here, B_1, B_2, k_1 and k_2 are modelling coefficients.

The growth rate is expressed by (Mersmann et al., 2001):

$$G = k_G(S - 1), \qquad (13)$$

which depends linearly on the supersaturation, assuming a diffusion-controlled growth. This is a reasonable assumption at high supersaturation ratios. In addition, k_G is a modelling coefficient. In this work, the growth rate is assumed independent from the particle size, but accounting for size-dependent growth rates is indeed possible.

Aggregation is assumed to occur due to the Brownian motions and turbulent fluctuations. The collision rates related to these two mechanisms are respectively described by the following expressions (Mersmann and Braun, 2001; Saffman and Turner, 1956):

$$\beta_{ij}^{Br} = \frac{2k_B T}{3\mu} \frac{(L_i + L_j)^2}{L_i L_j}, \qquad (14)$$

and

$$\beta_{ij}^{Turb} = C_T \pi \sqrt{\frac{8}{15}} \left(\frac{\varepsilon}{\nu}\right)^{0.5} (L_i + L_j)^3, \qquad (15)$$

where L_i and L_j are the size of the colliding particles and C_T is a correction term to account for deviations from the simplified theory adopted to derive the expression. In addition, k_B, μ and T denote the Boltzmann constant, liquid viscosity and temperature, respectively. Moreover, the following expression is used to estimate the aggregation efficiency under turbulent conditions (Bałdyga et al., 2003):

$$P_{ij} = \exp\left(-\frac{t_c}{t_i}\right), \qquad (16)$$

here, $t_i = \sqrt{\nu/\varepsilon}$ estimates the interaction time of two colliding particles under turbulent conditions, while, $t_c = \frac{D_b/f(\delta)}{G}$ is the time required for a bridge of diameter D_b to be formed between these particles. D_b and $f(\delta)$ are calculated following, respectively, the work by Bałdyga et al. (2003) and David et al. (1991):

$$D_b = \frac{\sqrt{\rho}(\varepsilon\nu)^{1/4}}{\sqrt{A_p}} \frac{L_i L_j}{\sqrt{L_i^2 + L_j^2 - L_i L_j}}, \qquad (17)$$

$$f_\delta = \frac{4(1 + \delta - \sqrt{\delta^2 - 1})}{1/3 + \delta - \sqrt{\delta^2 - 1} - (\delta - \sqrt{\delta^2 - 1})^2((2\delta + \sqrt{\delta^2 - 1})/3)}, \qquad (18)$$

where, A_p is a parameter that represents the yield strength of the particles and δ the particle size ratio and ρ the liquid density.

2.3. Chemical equilibria

As mentioned previously, supersaturation depends on the activity of the reactants, which are calculated from the chemical equilibrium. The reactions considered in the equilibrium calculation are those reported in Table 1, excluding the co-precipitation reaction.

The equilibrium concentrations are calculated by solving a system of non-linear equations that includes the equilibrium relation of each reaction, mass balance and electro-neutrality. The reaction constants are taken from the work by Van Bommel and Dahn (2009). The iterative Newton-Raphson method adapted to a system of equations is used for solving the equilibrium (Isaacson and Keller, 1966). Moreover, the activity coefficient is not included in the equilibrium calculation by observing the fact that the co-precipitation occurs at basic conditions (pH >10). As a result, the self-ionization of water has an insignificant contribution to the amount of OH⁻, and ammonia is negligibly dissociated at equilibrium conditions. For the complex formation reactions, the lack of data for ammonia-complex species leads us to assume the activity coefficients of the same order for the metal cations and their metal-ammonia complexes, because they have the same charge. However, the activity coefficients for the free metal cations and hydroxide ions are considered in the calculation of the supersaturation. A detailed explanation of the equilibrium calculation is provided in the Supplementary Material.

2.4. Activity coefficients

For the calculation of the supersaturation, Eq. (11), the product of activities for each metal hydroxide, $M(OH)_2$, is expressed as follows:

$$a_{M^{2+}}(a_{OH^-})^2 = [M^{2+}][OH^-]^2 \gamma_\pm^3, \qquad (19)$$

where, $\gamma_\pm$ is the mean molal activity coefficient. Here, the Bromley's method (Bromley, 1973) is adopted to calculate the mean molal activity coefficient for each pair of the cation metal and hydroxide ion in a multi-component solution. Moreover, the effect of ammonia on the activity coefficients is neglected. It is noteworthy that this method is valid up to ionic strengths of 6 M, which is the case of the operating conditions investigated in this work.

2.5. Calculation steps and simulation software

Fig. 1 depicts the calculation steps of the adopted approach for the steady-state simulation of the co-precipitation process.

The simulations are conducted by using the steady-state incompressible solver of the Ansys Fluent commercial software v202. In the simulations presented in this work, the flow field is solved first in a decoupled manner, since the particles are assumed to be passive, i.e., they do not influence the flow field. The reasoning behind this assumption is that the precipitated particles have sufficiently small size and their quantity results in a low volume fraction. Thus, they can be treated as passive particles due to their negligible inertia. Next, the transport equations (excluding the transient term) for p_i, $s_\alpha^{(4)}$ and $\langle m_k^{(4)} \rangle$ are solved simultaneously by defining them as user-defined scalars. The steady-state solver performs iterations until reaching the convergence that is detected by observing residuals for all the variables. In addition, some user-defined functions (UDF) are written to
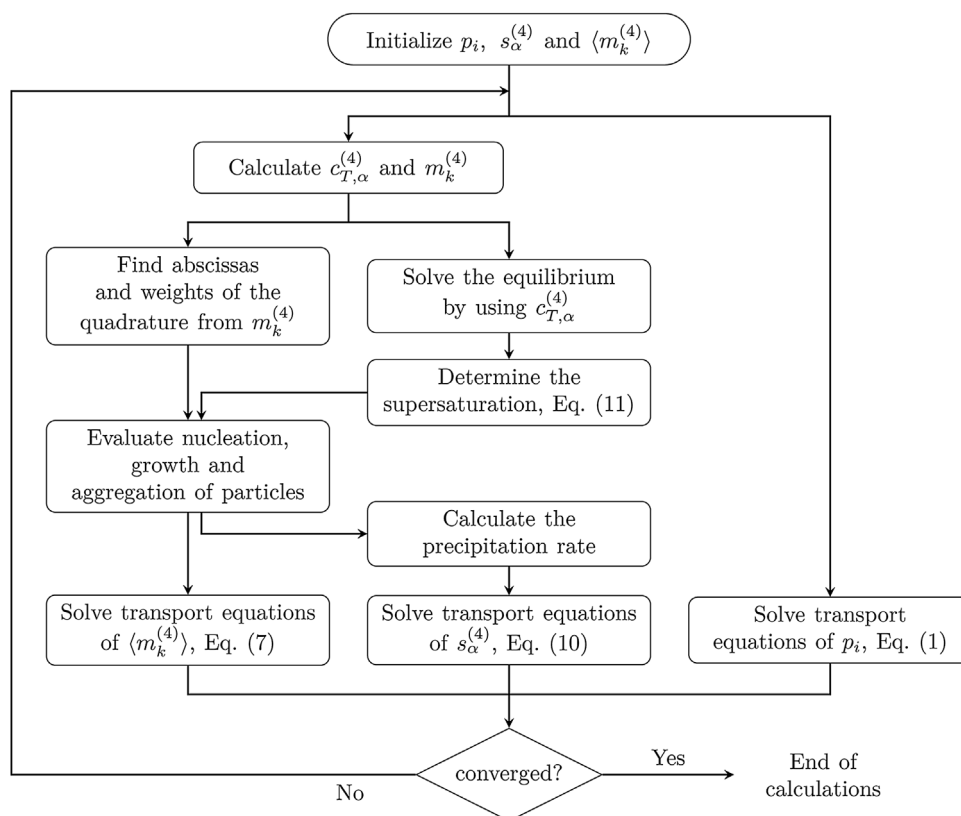
Fig. 1 – The calculation steps of the precipitation modelling.

solve the equilibrium, find the abscissas and weights of the quadrature, calculate the micromixing fluxes and determine the source terms required for the solution of the transport equations. These user-defined functions are shared by us on a public repository (Shiea et al., 2021). Moreover, in this work, the PSD is approximated by a 2-node quadrature that is determined by tracking four volume-weighted moments, $\langle m_k^{(4)} \rangle$, with k ranging between 0 and 3. It should be noted that the calculation of the abscissas and weights of the quadrature nodes is done by the 1-D adaptive quadrature technique (Yuan and Fox, 2011) based on the Chebychev algorithm (Wheeler, 1974). This technique allows running simulations with zero initial condition for the moments.

3. Results and discussion

As mentioned in the introduction, the CFD-PBE is used to simulate a multi-inlet vortex mixer (MIVM), depicted in Fig. 2. It consists of four inlet pipes of 1 mm diameter, a mixing chamber with a diameter of 4 mm and height of 1 mm, and an outlet pipe of 2 mm diameter and 41 mm length. Further details about the geometry discretization and computational mesh can be found in the Supplementary Material.

Concerning the operating conditions, the temperature is set to 25 °C, and the flow is assumed to exit at atmospheric pressure. The inlet metal concentrations and total inlet flow rate are varied to study their effect on the properties of precipitated particles, see Table 2. The inlet concentration of ammonia and sodium hydroxide is set such that the ratio between them and the inlet metal concentration is $[M^{2+}]:[NH_3]:[NaOH]=1:1:2$.

As shown in the previous section, the governing equations depend on the velocity field of the fluid. In addition, the micromixing and aggregation models depend on the tur-
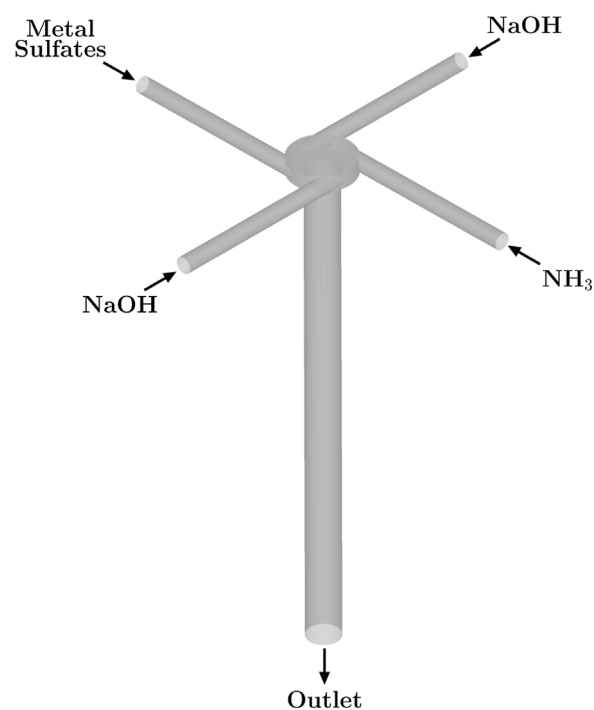

Fig. 2 – Sketch of the multi-inlet vortex mixer.

Table 2 – Summary of investigated operating conditions.

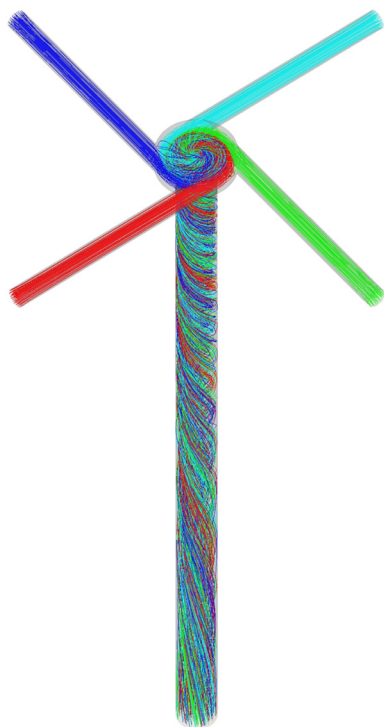| Total flow rate	Concentration (M)						
(mL/min)	0.01	0.02	0.04	0.1	0.2	0.4	1.0
50	×						×
70	×	×	×	×	×	×	×
105	×						×
170	×						×

Fig. 3 – Flow visualization by the pathlines of tracer particles released at the inlets. The pathline color shows the origin inlet of particles.

bulence parameters. This data is obtained by performing, in advance, a CFD simulation for each investigated total inlet flow rate. The CFD simulations are carried out by using the incompressible pressure-based steady solver of the Ansys Fluent commercial code. The turbulence is described by the SST $k - \omega$ model, adapted to low-Reynolds-number flows by introducing a damping coefficient for the turbulent viscosity. Concerning the boundary conditions, the normal velocity magnitude is imposed at the inlets, while the atmospheric pressure is set at the outlet. In addition, the *Radial Equilibrium Pressure Distribution* option is enabled for the pressure outlet condition to consider the radial profile of the static pressure in the rotating fluid at the outlet. Moreover, low turbulent intensity is specified at the inlets, since the inlet pipes operate at low Re number for all the investigated flow rates.

It is informative to visualize the fluid flow in the system. Fig. 3 shows the pathlines of some tracer particles released at the inlets. Inlet streams are distinguished by different colors. The pathlines illustrate that the inlet streams enter tangentially the mixing chamber, where they form a vortex that goes into the outlet pipe. The rotational motion developed in the mixing chamber persists in the outlet pipe, observed as helices near the wall. The pitch of helices increases with the distance from the outlet pipe entrance, which implies the decay of the rotational motion in the outlet pipe.

Further insight into the flow field can be gained from the profile of the axial velocity, i.e., z-component velocity, shown by Fig. 4. As it can be observed, an upward flow develops in the top center of the outlet pipe due to the pressure gradient induced by the fluid rotation. In contrast, the rotating fluid moves downward near the wall, as indicated by the blue sacks near the wall in the first part of the outlet pipe in Fig. 4. Then, as the flow moves towards the outlet, the downward flow spreads toward the center, and the rotating pattern near the wall broadens and decays.

The flow field can be also used to assess the assumption of sufficiently small particles that follow the fluid, particularly in the mixing chamber. In this work, the mean particle sizes are smaller than or in the order of the volume-averaged Kolmogorov length scale (10^{-5} m). Therefore, the particle Stokes number can be determined as the ratio of the particle time scale ($\frac{\rho_p L^2}{18 \rho v}$) and the Kolmogorov time scale (chosen as the fluid time scale), which turns out to be less than 1 (for flow rate of 70 mL/min). Here, L and ρ_p are the particle size and density, respectively. Moreover, it should be mentioned that the Kolmogorov time scale is the most conservative choice for the fluid time scale, because other (larger) time scales result in much smaller particle Stokes numbers. Since the Stokes number of particles is small (less than 1), it can be assumed that they follow the fluid flow.

After solving for the flow field, the governing equations, namely Eq. (1), Eq. (7), and Eq. (10), representing respectively micromixing, the PBE and species transport, are solved simultaneously. Let us start the discussion with the micromixing process. Fig. 5 shows the profiles of the environment probabilities for the total inlet flow rate of 70 mL/min. The profiles suggest that the mixing process occurs very quickly in the mixing chamber, i.e., the pure environments quickly mix to form the reacting environment. Therefore, the fluid can be considered as completely micro-mixed before entering the outlet pipe. It is noteworthy that despite the fast mixing process, the concentration of species in the reacting environment is not uniform. This spatial gradient of the concentrations will be illustrated later.

The mixing of the feed streams results in the formation of the reacting environment with the species activity higher than the solubility product. This activity in excess is indeed the supersaturation, which, triggers the formation of particles. Fig. 6 depicts the contour plots of the supersaturation for three inlet metal concentrations on the section that crosses the center of the mixing chamber and outlet pipe. For all the inlet concentrations, the highest supersaturation levels are observed in the mixing chamber, where the fresh feeds impinge. Then, the supersaturation decreases along the outlet pipe, since it is consumed by the co-precipitation of particles. As mentioned previously, the profiles of the total concentrations in the precipitation environment are not uniform in the mixing chamber, despite the fast mixing of the feeds. This behavior can be observed in the supersaturation contour plots shown in Fig. 6, which depend on the total concentrations of the precipitation environment.

Now, let us compare the supersaturation profiles of different inlet metal concentrations shown in Fig. 6. As expected, the larger the concentration of the species, the higher the supersaturation level is, as evidenced by the supersaturation values in the mixing chamber, where the highest levels of the supersaturation are observed. The comparison of the supersaturation level in the mixing chamber and at the outlet reveals that the supersaturation level falls rapidly (more than 99%) in the case of the high concentration (Fig. 6c), whereas, it decreases much less (around 34%) in the case of the low concentration (Fig. 6a). In fact, high supersaturation levels trigger the nucleation of a large number of nuclei, and these nuclei undergo the molecular growth that consumes the supersaturation quickly. However, in the case of low supersaturation levels, the nucleation of a significant number of nuclei takes longer, and therefore, the consumption of supersaturation by their molecular growth occurs over a longer period of time.
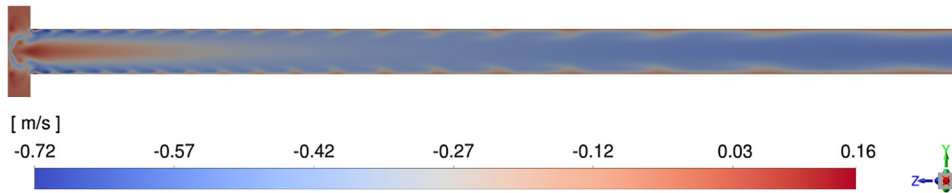
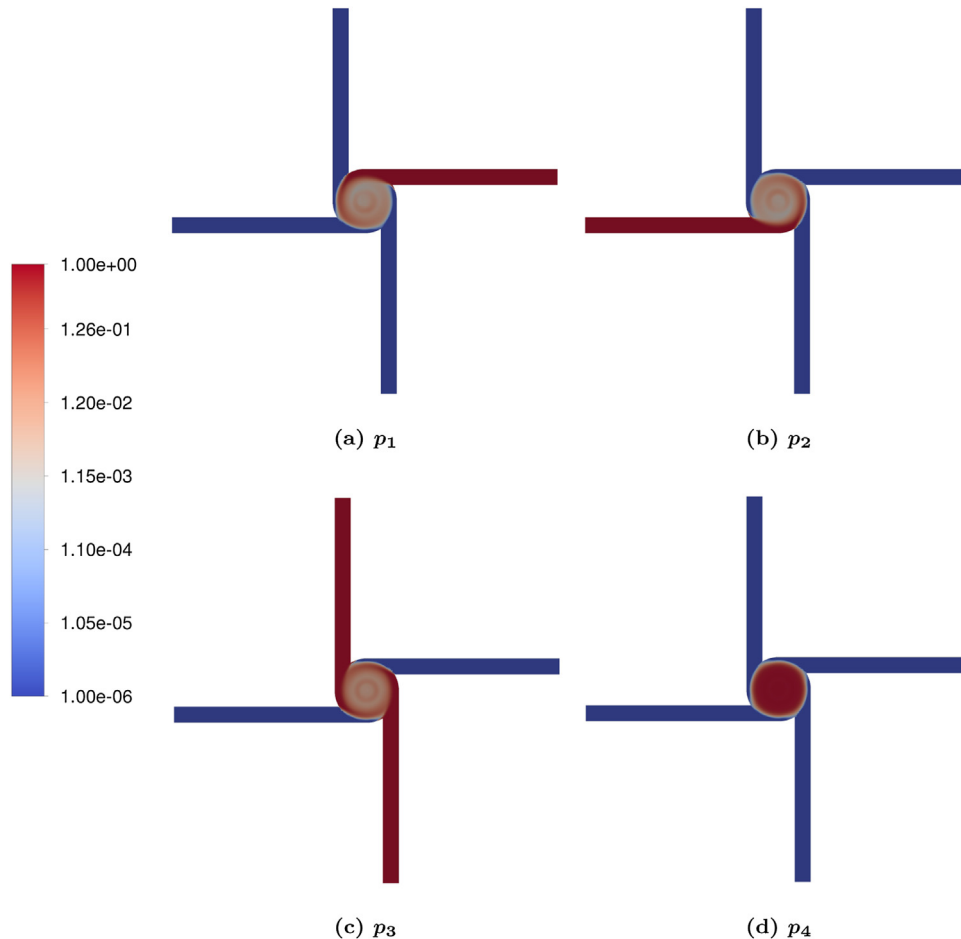**Fig. 4 – Contour plot of the z-component velocity (the total inlet flow rate is 70 mL/min).**

Fig. 5 – Environment probability profiles on the section that cuts through the middle of the mixing chamber and inlet pipes (the total inlet flow rate is 70 mL/min).

Concerning the co-precipitation of particles, let us consider the Sauter mean diameter (SMD), i.e., d_{32}, calculated as the ratio between the moments of order 3 and 2 with respect to particle size:

$$\text{SMD} = d_{32} = \frac{\langle m_3^{(4)} \rangle}{\langle m_2^{(4)} \rangle}. \tag{20}$$

Fig. 7 shows the obtained SMD profiles for three inlet metal concentrations on the same section depicted in Fig. 6. Here, SMD is calculated as the ratio of the surface-averaged $\langle m_3^{(4)} \rangle$ and $\langle m_2^{(4)} \rangle$. Let us start with the results related to the case with the lower concentration. As can be seen from Fig. 7a, micrometer particles are already formed in the mixing chamber, however, their number is too low to deplete the supersaturation by their growth in a time comparable to the residence time of the fluid in the mixing chamber. As the fluid flows in the outlet pipe, new particles are nucleated, and simultaneously, the existing particles grow. This growth results in the

increase of the SMD and a limited consumption of the supersaturation in the outlet pipe (see Fig. 6a). Another observation is the larger particle size near the walls and close to the mixer outlet. It is attributed to the higher dissipation rate in that area, which promotes the aggregation of particles, and the lower particle velocity, which increases the particle residence time. In contrast, a different pattern is observed for the case of high concentration. In this case, most of the supersaturation is consumed in the mixing chamber, leading to the formation of a large number of particles with small size. Eventually, the particles aggregate in the outlet pipe, leading to the further increase of the particle size. Moreover, the effect of the aggregation is expected to be much stronger in the case of high concentration, because the larger the number of particles, the higher the chance of their collision is, hence more aggregation. In fact, the volume-weighted average (in the mixing chamber and outlet pipe) of the aggregation frequency calculated between particles with a size equal to the SMD increases with the inlet metal concentration, as shown by Fig. 10.
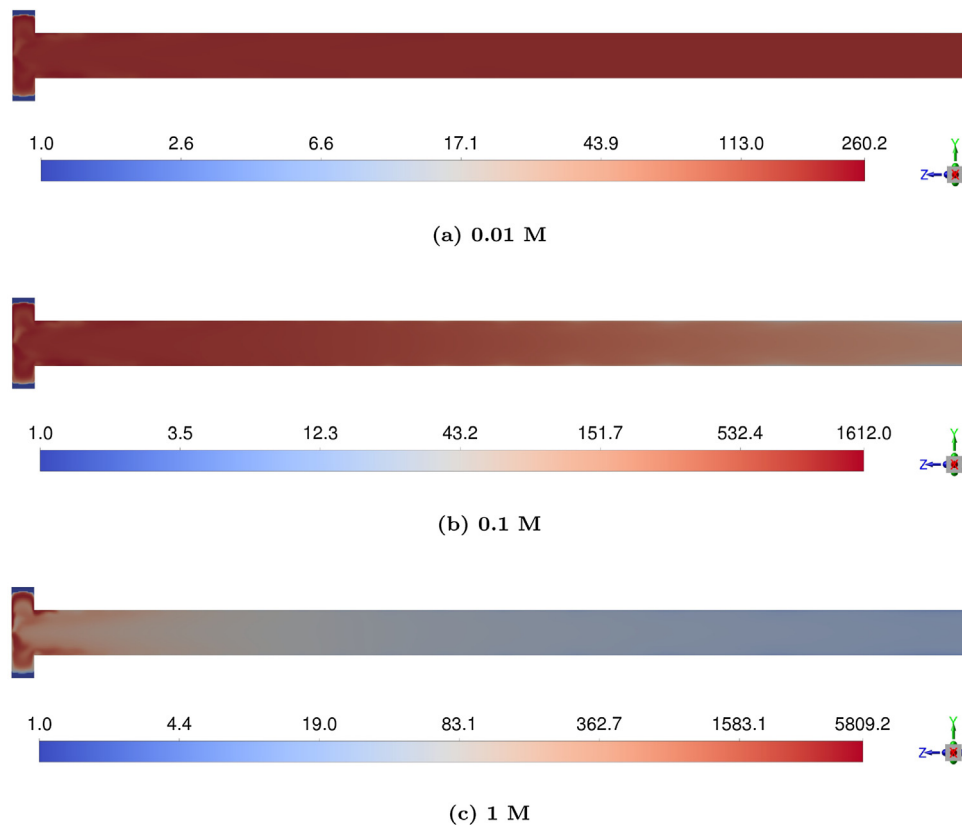
(a) 0.01 M

(b) 0.1 M

(c) 1 M

Fig. 6 – Contour plot of supersaturation for three inlet metal concentrations (total inlet flow rate is 70 mL/min).
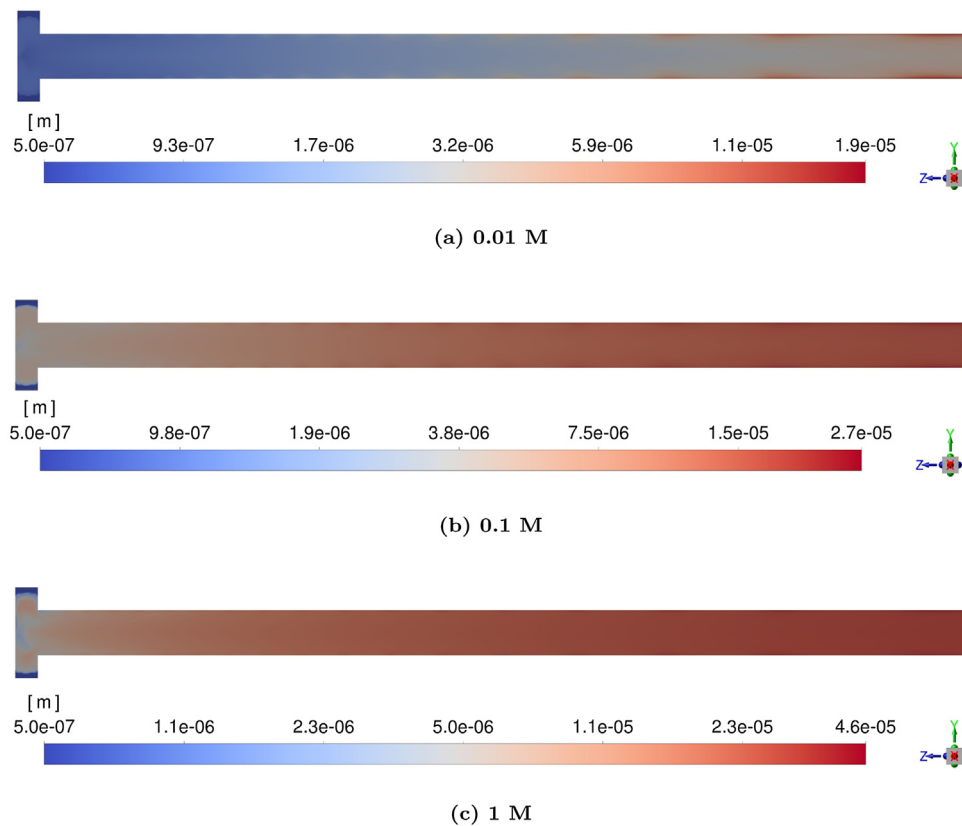

(a) 0.01 M

(b) 0.1 M

(c) 1 M

Fig. 7 – Contour plot of Sauter mean diameter (m) for three inlet metal concentrations (total inlet flow rate is 70 mL/min).

In the remainder of this section, the effect of two operating conditions, i.e., the total flow rate and inlet concentration, on the particle size at the outlet of the micromixer is discussed.

3.1. The effect of inlet flow rate

Fig. 8 plots the Sauter mean diameter at the outlet of the micromixer versus the total inlet flow rate for the low and high
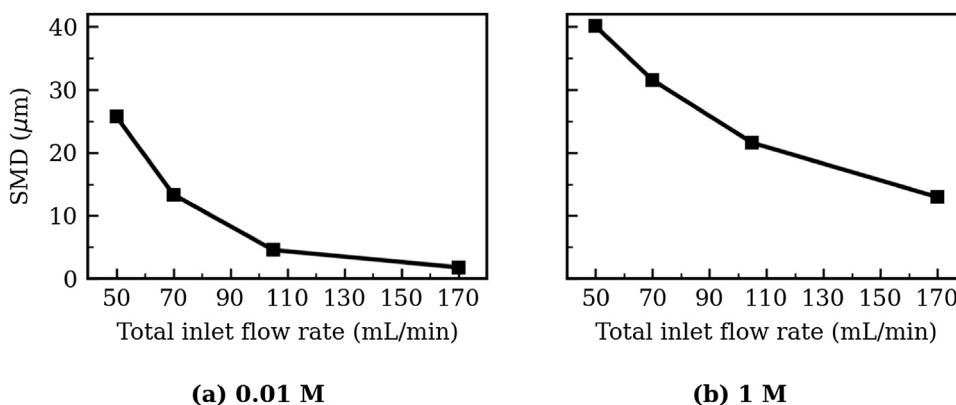
(a) 0.01 M   **(b) 1 M**

Fig. 8 – Mean values of Sauter mean diameter at the outlet of micromixer with respect to the total inlet flow rate for two inlet metal concentrations.

inlet metal concentrations. Here, the total inlet flow rate, i.e., the summation of the four equal inlet flow rates, is changed from 50 to 170 mL/min, corresponding to the Reynolds number of 4275 to 14535 in the mixing chamber, respectively. The Reynolds number in the mixing chamber is defined as follows (Bensaid et al., 2014; Cheng, 2010):

$$\text{Re} = \sum_{i=1}^{4} \frac{u_i D}{\nu}, \tag{21}$$

where, u_i, D, and ν denote the velocity of each inlet, diameter of the mixing chamber and kinematic viscosity of the liquid, respectively. As can be seen from Fig. 8, the SMD of particles reduces by the increase of the flow rate. This behaviour can be explained by considering two key factors that depend on the flow rate, i.e., turbulence intensity and residence time. On one hand, the increase of the flow rate intensifies the turbulence in the micromixer, which in turn, influences mixing and aggregation. On the other hand, the increase of the flow rate reduces the particle residence time, in other words, less growth and aggregation of particles. As long as mixing is concerned, intense turbulent conditions generally reduce the mixing time, i.e., accelerate the mixing. Moreover, the faster is mixing, the higher are the concentrations in the reacting environment, hence higher levels of supersaturation. As a consequence, more nucleation is expected by the increase of the flow rate, which eventually can contribute to the decrease of the particle size. However, as shown previously, micromixing occurs very quickly in this particular setup, implying that it may have a modest effect on the precipitation as a rate-controlling step, except at very high concentrations that the nucleation and growth rates, i.e., the precipitation rate, are very fast. In fact, this is verified by evaluating the change in the particle size predicted under the assumption of perfect micromixing for different concentrations, see Fig. S2 of the Supplementary material. Thus, micromixing can make only a slight contribution to the decreasing trend of the mean particle size in Fig. 8, particularly in the case of low concentration. However, this statement should be treated carefully as it depends on the nucleation and growth kinetic rates assumed in this work. In other words, if faster kinetic rates were employed, the role of micromixing could be more influential, even at low concentrations. In contrast, turbulence has a dual effect on aggregation. The increase of turbulent intensity promotes particle collisions, but simultaneously reduces the probability of two particles aggregating due to the decrease of

the contact time between them. This means that the increase of the flow rate can indeed reduce the aggregation of the particles under specific conditions. In addition, it can decrease the time in which particles can aggregate by reducing the residence time. Now let us summarize the role of these factors for each case shown in Fig. 8. In the case of high concentration (Fig. 8b), the decreasing trend is mainly due to the reduction of the aggregation, which is caused by the increase of the turbulence intensity and the decrease of the residence time. In the case of low concentration, as explained before, the effect of aggregation is limited since the number of particles is lower in comparison with that of the high-concentration case. Instead, in this case, the particles are being nucleated and then grow through the entire micromixer. Therefore, the decreasing trend of the particle size can be associated with the decrease of the residence time, i.e., reduction of the time in which the particles grow.

3.2.   The effect of inlet metal concentration

The inlet metal concentration is varied between 0.01 M and 1 M to investigate its effect on the predicted PSD and SMD. It is worth repeating that the concentration of other inlets is varied accordingly in order to respect the concentration ratio of $[M^{2+}]$:$[NH_3]$:$[NaOH]$=1:1:2. Moreover, the total flow rate is set to 70 mL/min.

First, it is useful to analyze the PSD at the outlet of the micromixer. It is noteworthy that the control of the PSD (generally desired to be narrow (Barai et al., 2019; Wang et al., 2011)) is of fundamental importance in the manufacturing of precursors for cathode material. In this work, the PSD is reconstructed from the moments averaged over the outlet surface, assuming a specific shape for the distribution; here the log-normal shape is used. This choice is made to approximate the PSD for the sake of comparison, and not to imply the shape of the true underlying PSD. The reconstructed PSDs at the outlet of the micromixer are reported in Fig. 9 for three inlet metal concentrations. It is evident that the PSD becomes wider as the inlet metal concentration increases, which can be associated to the effect of the aggregation, as explained previously. Indeed, the strong effect of the aggregation at high concentrations can be evidenced by plotting the volume-weighted average (in the mixing chamber and outlet pipe) of the aggregation frequency versus the inlet metal concentration, see Fig. 10.

Now, we turn our attention to the average particle size and particle number density. Fig. 11 shows the Sauter mean

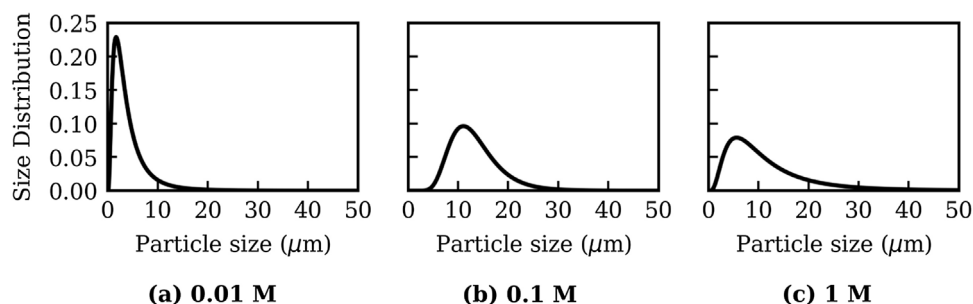**(a) 0.01 M**   **(b) 0.1 M**   **(c) 1 M**

Fig. 9 – Reconstructed particle size distribution at the outlet of the micromixer for three inlet metal concentrations (total inlet flow rate is 70 mL/min).
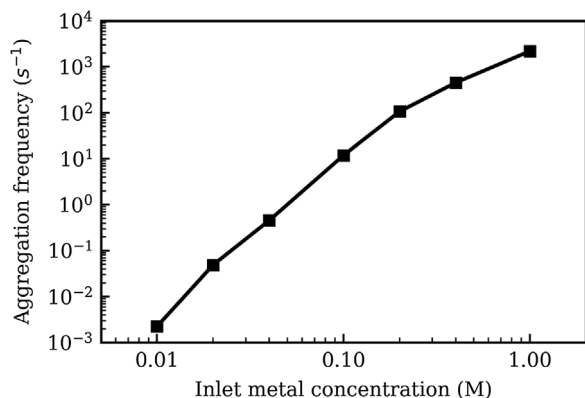

Fig. 10 – Volume-weighted average (in the mixing chamber and outlet pipe) of the aggregation frequency between two particles of size equal to the SMD versus the inlet metal concentration.
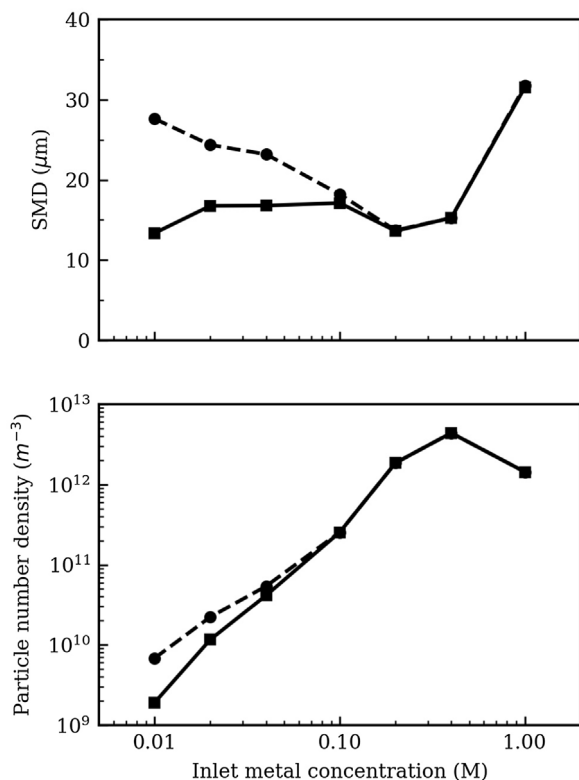

Fig. 11 – Sauter mean diameter, SMD, (top) and particle number density (bottom) at the outlet of the micromixer (solid curves) versus the inlet metal concentration (total inlet flow rate is 70 mL/min). The dashed-curves represent the predictions after the consumption of the supersaturation by the simplified model.

diameter and particle number density at the outlet of the micromixer (solid curves) versus the inlet metal concentration. At first glance, it seems that the particle size becomes larger by increasing the concentration. However, it is explained previously that, in the cases of low concentration, the supersaturation level at the outlet is still significant with respect to the maximum level generated in the mixing chamber. This means that the particle size is expected to increase further in these cases, provided that the co-precipitation is allowed to continue until the depletion of the supersaturation. In contrast, in the cases of high concentration, a significant amount of the supersaturation generated in the mixing chamber is consumed before the fluid reaches the outlet, which results also in a considerable solid concentration at the outlet. Therefore, a better comparison can be offered by continuing the co-precipitation until the complete depletion of the supersaturation in all the cases. Here, it is done by employing a simplified model of mixed batch co-precipitation, initialized with the average values at the outlet of the micromixer. One can think of it as collecting the solution at the outlet of the micromixer in a stirred beaker wherein the supersaturation depletes completely. Essentially, the simplified model performs similar calculation steps as the full model, see Fig. 1, but the governing equations, i.e., Eq. (1), Eq. (7), and Eq. (10), do not include any term that depends on the spatial coordinates, and they are integrated by a solver for ordinary differential equations until depleting the supersaturation ($S \approx 1$). Moreover, no aggregation contribution is assumed in the simplified model, since it depends on turbulence modelling. The corresponding results are shown in Fig. 11 by the dashed curves. As expected, the particle size and number density change only at low concentrations, for which a large portion of the supersaturation generated in the mixing chamber exit from the outlet. On the contrary, at high concentrations, the remaining supersaturation at the outlet of the micromixing can barely change the particles size and number density of the already precipitated (large) population of particles. It is interesting to see that the particle size presents a minimum as the concentration increases (dashed curve in the top plot of Fig. 11). First, the particle size versus the concentration follows a decreasing trend, which is associated with the fact that the higher the concentration, the higher the supersaturation level is. As a consequence, more particles are nucleated with the increase of the concentration (as shown by the bottom plot in Fig. 11), which eventually reduces the growth of individual particles. However, this trend inverses with the further increase of the concentration (i.e., supersaturation) because the number of particles increases to a significant extent that considerably boosts the aggregation, as indicated previously by Fig. 10. Indeed, a strong effect of aggregation at concentration 1 M

results in a sharp increase of the SMD and a decrease of the particle number density, see Fig. 11.

To conclude, we believe that the observed trend of SMD deserves to be investigated experimentally, and it can be leveraged in studying models for the nucleation, growth and aggregation of Ni-Mn-Co hydroxide particles.

4. Conclusions

In this work, a comprehensive modelling framework based on the CFD-PBE is proposed to simulate the co-precipitation of Ni-Mn-Co hydroxide. The CFD provides information about the fluid dynamics, while the PBE describes the formation and evolution of particles by the nucleation, growth and aggregation. In addition, the framework includes an equilibrium solver to estimate the supersaturation level, and also, a micromixing model to take into account the mixing process as a potentially controlling step in fast reacting systems.

The approach is used to simulate the co-precipitation of $Ni_{0.8}Mn_{0.1}Co_{0.1}(OH)_2$ in a multi-inlet vortex mixer as the case study. Interesting trends have been observed for the outlet particle size by changing the operating conditions such as the flow rate and inlet concentration. For instance, a decreasing trend has been observed for the Sauter mean diameter at the outlet as the inlet flow rate increases. As another example, the Sauter mean diameter has presented a minimum value as the inlet concentration has been increased at a fixed inlet flow rate. The former has been associated with the effect of the turbulence intensity and residence time on the particle co-precipitation, whereas the latter has indicated the interplay of the nucleation, growth and aggregation in the increase of the particle size. We believe that the effect of the nucleation, growth and aggregation on the particle formation can be assessed and studied further by conducting experiments in similar systems, and by examining particle properties, such as the mean size, size distribution, morphology and crystal structure. Indeed, such investigations can leverage the proposed modelling framework to develop kinetic models for the nucleation and growth of Ni-Mn-Co hydroxide crystals by matching the measured and predicted particle sizes. Moreover, this modelling framework can be adopted to simulate pilot-scale continuous systems, e.g., CSTRs, provided that reliable kinetic models are available for the particle nucleation and growth. These subjects are planned to be explored in our next works.

Author's contribution

M. Shiea: Conceptualization, Methodology, Software, Formal analysis, Validation, Visualization, Writing – Original Draft; **A. Querio**: Software, Formal analysis, Validation, Visualization, Writing – Original Draft; **A. Buffo**: Conceptualization, Writing – Review & Editing, Supervision; **G. Boccardo**: Conceptualization, Writing – Review & Editing, Supervision; **D. Marchisio**: Conceptualization, Writing – Review & Editing, Project administration, Funding acquisition.

Declaration of Competing Interest

The authors declare that they have no known competing financial interests or personal relationships that could have appeared to influence the work reported in this paper.

Acknowledgement

Appendix A. Supplementary Data

Supplementary data associated with this article can be found, in the online version, at https://doi.org/10.1016/j.cherd.2021.11.008.

References

Bałdyga, J., Jasińska, M., Orciuch, W., 2003. Barium sulphate agglomeration in a pipe-an experimental study and CFD modeling. Chem. Eng. Technol. 26 (3), 334–340.

Barai, P., Feng, Z., Kondo, H., Srinivasan, V., 2019. Multiscale computational model for particle size evolution during coprecipitation of li-ion battery cathode precursors. J. Phys. Chem. B 123 (15), 3291–3303.

Bensaid, S., Deorsola, F., Marchisio, D., Russo, N., Fino, D., 2014. Flow field simulation and mixing efficiency assessment of the multi-inlet vortex mixer for molybdenum sulfide nanoparticle precipitation. Chem. Eng. J. 238, 66–77.

Bromley, L.A., 1973. Thermodynamic properties of strong electrolytes in aqueous solutions. AIChE J. 19 (2), 313–320.

Cheng, J.C., Fox, R.O., 2010. Kinetic modeling of nanoprecipitation using CFD coupled with a population balance. Ind. Eng. Chem. Res. 49 (21), 10651–10662.

Cheng, J.C., 2010. A Comprehensive Model Study for Flash Nanoprecipitation: Computational Fluid Dynamics, Micro-Particle Image Velocimetry, and Population Balance Modeling. Iowa State University, Ph.D. thesis.

David, R., Marchal, P., Klein, J.-P., Villermaux, J., 1991. Crystallization and precipitation engineering-III. a discrete formulation of the agglomeration rate of crystals in a crystallization process. Chem. Eng. Sci. 46 (1), 205–213.

Deng, C., Liu, L., Zhou, W., Sun, K., Sun, D., 2008. Effect of synthesis condition on the structure and electrochemical properties of $Li[Ni_{1/3}Co_{31/3}Mn_{1/31/3}]O_2$ prepared by hydroxide co-precipitation method. Electrochimica. acta 53 (5), 2441–2447.

Fox, R.O., 1998. On the relationship between lagrangian micromixing models and computational fluid dynamics. Chem. Eng. Process. 37 (6), 521–535.

Isaacson, E., Keller, H.B., 1966. Analysis of Numerical Methods. Wiley.

Kim, J.-M., Chang, S.-M., Chang, J.H., Kim, W.-S., 2011. Agglomeration of nickel/cobalt/manganese hydroxide crystals in couette-taylor crystallizer. Colloids Surf. A 384 (1-3), 31–39.

Lee, M.-H., Kang, Y.-J., Myung, S.-T., Sun, Y.-K., 2004. Synthetic optimization of $Li[Ni_{1/31/3}Co_{1/31/3}Mn_{1/31/3}]O_2$ via co-precipitation. Electrochim. Acta 50 (4), 939–948.

Lince, F., Marchisio, D.L., Barresi, A.A., 2011. A comparative study for nanoparticle production with passive mixers via solvent-displacement: use of CFD models for optimization and design. Chem. Eng. Process. 50 (4), 356–368.

Liu, Y., Fox, R.O., 2006. CFD predictions for chemical processing in a confined impinging-jets reactor. AIChE J. 52 (2), 731–744.

Liu, Y., Cheng, C., Prud'homme, R.K., Fox, R.O., 2008. Mixing in a multi-inlet vortex mixer (MIVM) for flash nano-precipitation. Chem. Eng. Sci. 63 (11), 2829–2842.

Liu, L., Yang, X., Yang, J., Li, G., Guo, Y., Xue, C., 2021. Modelling of turbulent shear controllable co-precipitation synthesis of lithium ion battery cathode precursor micro-particles in a taylor-couette flow reactor with variable configurations of inner cylinder. Chem. Eng. J. 411, 128571.

Marchisio, D.L., Fox, R.O., 2013. Computational Models for Polydisperse Particulate and Multiphase Systems. Cambridge University Press.

Marchisio, D., Barresi, A., Fox, R., 2001. Simulation of turbulent precipitation in a semi-batch taylor-couette reactor using CFD. AIChE J. 47 (3), 664–676.

Marchisio, D.L., Barresi, A.A., Garbero, M., 2002. Nucleation, growth, and agglomeration in barium sulfate turbulent precipitation. AIChE J. 48 (9), 2039–2050.

Marchisio, D.L., Pikturna, J.T., Fox, R.O., Vigil, R.D., Barresi, A.A., 2003. Quadrature method of moments for population-balance equations. AIChE J. 49 (5), 1266–1276.

Marchisio, D.L., Omegna, F., Barresi, A.A., Bowen, P., 2008. Effect of mixing and other operating parameters in sol- gel processes. Ind. Eng. Chem. Res. 47 (19), 7202–7210.

Mersmann, A., Braun, B., 2001. Agglomeration. In: Crystallization Technology Handbook, 2nd Edition. Marcel Dekker, Inc, pp. 249–298.

Mersmann, A., Eble, A., Heyer, C., 2001. Crystal growth. In: Crystallization Technology Handbook, 2nd Edition. Marcel Dekker, Inc, pp. 95–158.

Mersmann, A., 2001. Physical and chemical properties of crystalline systems. In: Crystallization Technology Handbook, 2nd Edition. Marcel Dekker, Inc, pp. 1–44.

Pohorecki, R., Baldyga, J., 1983. New model of micromixing in chemical reactors. 1. general development and application to a tubular reactor. Ind. Eng. Chem. Fundam. 22 (4), 392–397.

Saffman, P., Turner, J., 1956. On the collision of drops in turbulent clouds. J. Fluid Mech. 1 (1), 16–30.

Shiea, M., Querio, A., Buffo, A., Boccardo, G., Marchisio, D., 2021. Simulation of Ni-Mn-Co Hydroxide Co-Precipitation by the CFD-PBE Approach. https://github.com/mulmopro/wet-synthesis-route/tree/main/cfd_pbe_fluent_udf.

Van Bommel, A., Dahn, J., 2009. Analysis of the growth mechanism of coprecipitated spherical and dense nickel, manganese, and cobalt-containing hydroxides in the presence of aqueous ammonia. Chem. Mater. 21 (8), 1500–1503.

Volmer, M., Weber, A., 1926. Keimbildung in übersättigten gebilden. Zeitschrift für Physikalische Chemie 119U (1), 277–301.

Wang, D., Belharouak, I., Koenig, G.M., Zhou, G., Amine, K., 2011. Growth mechanism of $Ni_{0.3}Mn_{0.7}CO_3$ precursor for high capacity li-ion battery cathodes. J. Mater. Chem. 21 (25), 9290–9295.

Wheeler, J.C., 1974. Modified moments and Gaussian quadratures. Rocky Mt. J. Math. 4, 287–296.

Yang, Y., Xu, S., Xie, M., He, Y., Huang, G., Yang, Y., 2015. Growth mechanisms for spherical mixed hydroxide agglomerates prepared by co-precipitation method: a case of $Ni_{1/3}Co_{1/3}Mn_{1/3}(OH)_2$. J. Alloys Compd. 619, 846–853.

Yuan, C., Fox, R.O., 2011. Conditional quadrature method of moments for kinetic equations. J. Comput. Phys. 230, 8216–8246.